Title	Nonhomogeneous spatial distribution of filamentary leakage current paths in circular area Pt/HfO2/Pt capacitors
Authors	Miranda, Enrique;Jiménez, David;Suñé, Jordi;O'Connor, Éamon;Monaghan, Scott;Povey, Ian M.;Cherkaoui, Karim;Hurley, Paul K.
Publication date	2013
Original Citation	MIRANDA, E., JIMENEZ, D., SUNE, J., O'CONNOR, E., MONAGHAN, S., POVEY, I., CHERKAOUI, K. & HURLEY, P. K. 2013. Nonhomogeneous spatial distribution of filamentary leakage current paths in circular area Pt/HfO[sub 2]/Pt capacitors. Journal of Vacuum Science & Technology B: Microelectronics and Nanometer Structures, 31, 01A107-6. http://dx.doi.org/10.1116/1.4768681
Type of publication	Article (peer-reviewed)
Link to publisher's version	10.1116/1.4768681
Rights	© 2013 American Vacuum Society. This article may be downloaded for personal use only. Any other use requires prior permission of the author and the American Vacuum Society. The following article appeared in MIRANDA, E., JIMENEZ, D., SUNE, J., O'CONNOR, E., MONAGHAN, S., POVEY, I., CHERKAOUI, K. & HURLEY, P. K. 2013. Nonhomogeneous spatial distribution of filamentary leakage current paths in circular area Pt/HfO[sub 2]/Pt capacitors. Journal of Vacuum Science & Technology B: Microelectronics and Nanometer Structures, 31, 01A107-6. and may be found at http://dx.doi.org/10.1116/1.4768681
Download date	2024-12-14 07:35:48
Item downloaded from	https://hdl.handle.net/10468/1647

University College Cork, Ireland
Coláiste na hOllscoile Corcaigh

Non-homogeneous Spatial Distribution of Filamentary Leakage Current Paths in Circular Area Pt/HfO_2/Pt Capacitors

E. Miranda, D. Jiménez, J. Suñé

Departament d'Enginyeria Electrònica, Universitat Autònoma de Barcelona, 08193 Cerdanyola del Valles, Spain

E. O'Connor, S. Monaghan, I. M. Povey, K. Cherkaoui, and P.K. Hurley

Tyndall National Institute, University College Cork, Lee Maltings Complex, Prospect Row, Cork, Ireland

ABSTRACT

The spatial distribution of filamentary leakage current paths in circular area Pt/HfO_2/Pt capacitors generated as the result of severe electrical stress is investigated using 2D statistical methods. The filamentary paths are associated with important thermal effects occurring inside the HfO_2 layer and manifest externally as a random spot pattern on the top Pt electrode. It is shown in this paper that for the largest area devices available a significant departure from homogeneity is detected close to the periphery of the structures. The observed deviation consists in a lower density of spots than that expected for a homogeneous Poisson process. Even though the ultimate reason for this anomaly is still under investigation, the obtained results demonstrate that the frequently assumed hypothesis in oxide reliability analysis of complete spatial randomness should not always be taken for granted.

Keywords: oxide breakdown, reliability, MIM, resistive switching

Corresponding author: enrique.miranda@uab.cat

I. INTRODUCTION

It is frequently assumed in oxide reliability analysis that the spatial distribution of breakdown (BD) events in metal-insulator-metal (MIM) and metal-insulator-semiconductor (MIS) obeys the precepts of a Poisson point process, that is: *i)* the *number* of points falling in any region *A* has a Poisson distribution, *ii)* given that there are *n* points inside a region *A*, the locations of these points are uniformly distributed inside *A*, and *iii)* the contents of two disjoint regions *A* and *B* are independent [1]. One of the major consequences of *i)-iii)* is that the occurrence of a single event in many small areas is totally equivalent to the occurrence of multiple events in a single large area. This is the basis for reliability extrapolation to total circuit area [2]. Interactions between points or *hidden* features of the region or sub-regions within which the points are generated are completely disregarded. In terms of hypothesis testing, *i)-iii)* defines the basic reference or null model of a point process in the plane, often referred to in the specialized literature as the Complete Spatial Randomness (*CSR*) process [1].

In practice, oxide reliability analysis is carried out on a large number of small area devices using the so-called time-dependent dielectric breakdown (TDDB) test, which consists in applying a constant voltage/current stress to the devices and record the time to the first current/voltage jump detected during the measurement. This event can be identified with the partial (soft BD) or complete (hard BD) formation of a filamentary leakage current path running across the dielectric layer [3]. It has been reported several times that the time-to-BD (t_{BD}) statistics, be it soft or hard BD, follow the Weibull distribution with shape parameter β [4]. Even after this first event, and under certain circumstances, successive BD events can be recorded but the interpretation of the results requires invoking the order statistics theory [5]. In oxide reliability analysis this is called successive BD statistics and corresponds to the opening

of multifilamentary conduction paths [6]. In ultrathin oxides (<2 nm), the current or voltage drift becomes progressive so that the above mentioned jumps are no longer observed. In this case the current/voltage evolution corresponds to the gradual opening of a single filamentary path and the failure criterion changes from t_{BD} to the time-to-current/voltage level [7]. This latest case will not be covered here.

TDDB test not only provides information about the temporal occurrence of BD events in MIM and MIS structures but also gives insight about their spatial distribution. The issue has major reliability implications since the device lifetime is expected to be sensitive to the degree of spatial correlation among BD spots [8]. To assess whether the BD spots follow a *CSR* process or not, two approaches are commonly followed: firstly, one can infer their spatial distribution from the t_{BD} Gumbel plot [2,6] (this is the standard approach), or secondly, one can analyze the locations of a large number of spots in a single large area device [8]. Concerning the first method, the experimental fact that the slope β is independent of the device area is well known to be a consequence of the Poisson area scaling [2]. This approach often relies on the detection of a single BD event per device so that it precludes exploring non-homogeneities. Successive breakdown statistics has also be found consistent with *CSR* but, again, the analysis is limited in practice to a few events per device [6]. In connection with the second method, in [8], the correlation among spots in a large area device was evaluated using simulated data compatible with the current distribution in a four-terminal device fabricated to that aim. The authors found that the BD spots do not exhibit spatial correlation effects and therefore that they follow a homogeneous Poisson point process. In view of the published results, *CSR* seems to be the rule for the conductive filaments or BD spots generation in MIM and MIS devices so that it would be worth investigating whether this is always the case or not.

In this paper, experimental results demonstrating that the hypothesis of a *CSR* process for the BD spots generation does not always hold are reported. The deviation is particularly important in some of our devices, those which allow examining a large number of failure events. Here, instead of using the electrical localization methods discussed above, direct visualization will be considered. Thanks to the thermal processes that come along with the formation of the filamentary paths across the HfO_2 layer, permanent marks on the top Pt electrode associated with extreme power dissipation effects allows identifying the location of the BD spots with high accuracy. The spot pattern is subsequently analyzed using a variety of 2D spatial statistics methods, all of them included in the Spatstat package for the R language [9].

II. THE DEVICES

The devices were fabricated as follows: a 200 nm-thick thermal SiO_2 is grown on n-type Si(100) substrates with resistivity of 1-4 Ω.cm. MIM capacitors are formed on this insulating layer by firstly depositing Pt (200 nm) by electron-beam (e-beam) evaporation. The samples are then placed in a Cambridge NanoTech Fiji atomic layer deposition (ALD) system where HfO_2 (30 nm) is deposited using TEMAHf precursor and H_2O. The samples are then returned to the e-beam evaporator and a Pt layer (200 nm) is deposited on top of the HfO_2. Lithography and a lift-off process are used to form arrays of circular area capacitors with different radius. Access to the bottom Pt metal is enabled via a dry etching technique using a mask/resist process that removes the HfO_2 to the bottom Pt metal while at the same time protecting the top Pt metal of the patterned devices. In addition, the oxide extends 25 μm beyond the perimeter edge of the top metal. The κ-value range estimated from capacitance-voltage measurements (not shown here) is around 20-21.

III. EXPERIMENTAL RESULTS AND DISCUSSION

The application of positive voltage ramps to the top metal electrodes of our MIM capacitors generates a large number of spots as illustrated in Fig. 1. In this particular case a voltage ramp from 0 V to 10 V was applied to a sample with radius R=169 μm. The generation of spots over the Pt plate is associated with a notable increase of the leakage current that flows through the structure. After the appearance of the BD spots the current is so large that it exceeds the measurement limit of the experimental setup (100 mA). For illustrative purposes, several devices with different size (R=113, 225, 282, and 423 μm) before and after the electrical stress are shown in Fig. 2. The outer dark ring corresponds to the extension of the dielectric layer. From these photographs it is possible to locate the BD spots and record their positions for subsequent analysis. In what follows, the spot pattern will be mathematically treated as a point pattern. As discussed in [10], it is important to have in mind that even in the absence of actual interactions among the filamentary paths, some deviation from *CSR* may arise as a consequence of *environmental* variations (in our case oxide thickness, permittivity, extrinsic defects, strain, etc.) leading to device regions with relatively high or low concentrations of events. On the contrary, the observation of *CSR* can help us to rule out such environmental variations as well as interpoint interactions.

As a first step, the interpoint distances will be statistically assessed. Figure 3.a and 3.b show interpoint distance histograms for a set of devices with different areas. In this case, the distances from every point to the rest is evaluated. If N is the number of points considered, the number of distances is $N(N\text{-}1)/2$. The solid lines were calculated from the theoretical probability distribution for a *CSR* process given by the expression:

$$f_{CSR}(x) = \frac{2x}{R^2}\left[\frac{2}{\pi}\cos^{-1}\left(\frac{x}{2R}\right) - \frac{x}{\pi R}\sqrt{1-\frac{x^2}{4R^2}}\right] \qquad 0 < x < 2R \qquad (1)$$

where x is the interpoint distance and R the device radius. Eq.(1) can be derived from Crofton's fixed point theorem using geometrical arguments [11]. As shown in Fig. 3.a, the *CRS* model nicely fits the empirical histograms for the four smallest device areas available (R=56 μm, 113 μm, 169 μm, 225 μm), which is in total agreement with previous studies [2,6,8]. On the contrary, as illustrated in Fig. 3.b, the *CRS* model (solid lines) cannot account for the empirical histograms for the two largest area devices (R=282 μm, 423 μm). The deviation is particularly important for the longest distance range. A similar departure from *CSR* occurs for the nearest neighbor distributions as shown in Fig. 4.b. In this case the solid lines are given by the expression [1]:

$$h_{CSR}(w) = 2\lambda\pi w \exp\left(-\lambda\pi w^2\right) \qquad 0 < w < 2R \qquad (2)$$

where w is the interpoint distance and λ is the intensity of the point process, *i.e.* the average number of points per unit area. The fact that there is an anomaly with the two largest area devices investigated is clearly detected when the median of the interpoint distances M is plotted as a function of R. In Fig. 5, the experimental data are the black symbols while the theoretical linear relationship for a *CSR* process M=0.905R is represented by the solid line [12]. The number of spots N counted in each case is also indicated. Notice that whereas the first four symbols lay over the theoretical line, the symbols corresponding to the two largest areas are below the solid line, *i.e.* the experimental median is less than what is theoretically expected. Even though the agreement improves if the number of spots N increases (by means of the application of

additional stress to the same device), there is still a significant difference (see Fig. 5). This deviation can also be found in the empirical histograms shown in Fig. 3.b as a small shift towards the shortest distances range. According to these observations the *CSR* model can be ruled out for our largest area devices.

The origin of the detected anomaly can be found in the non-homogeneous distribution of spots revealed by the intensity plots shown in Fig. 6. The use of different bandwidths *BW* for the Gaussian kernel implemented to calculate the local intensity maps allows identifying a region close to the periphery of the device (R=424 μm) with a lower number of spots than the one corresponding for a homogeneous Poisson process. A similar conclusion can be drawn from the analysis of the radial distribution of spots illustrated in Fig. 7. Figures 7.a and 7.b correspond to different degradation stages of the same device. In both figures, the empirical histograms are below the theoretical distribution for a *CSR* process (solid lines) for r values close to R. In this case, the theoretical expression for the radial distribution of points is given by the simple expression [1]:

$$q_{CSR}(r) = \frac{2r}{R^2} \qquad 0 < r < R \tag{3}$$

where r is the distance of the point measured from the center of the disc.

There is wide consensus in the statistical community that the most important functional summary estimator available for point patterns is the pair correlation function *g(r)*. This function is defined as the probability of observing a pair of points separated by a distance r divided by the corresponding probability for a homogeneous Poisson

process. It can be demonstrated that for a *CSR* process $g_{CSR}(r)=1$, while, in general, $g(r)>1$ suggests clustering or attraction and $g(r)<1$ suggests inhibition or regularity [1]. It is important to take into account that the estimator g fails for r values close to 0. Figure 8 illustrates $g(r)$ for the devices under investigation. It is clearly seen that the curves corresponding to the devices with radius R=282 μm and R=423 μm are approximately constant and slightly above the *CSR* reference line ($g_{CSR}(r)=1$). Although this can be interpreted at first sight as a kind of aggregation effect, it is in fact a consequence of the lower density of spots in the periphery of the devices. The points seem to concentrate in a smaller area, different from the actual device area. Interestingly, as illustrated in Fig. 9, the theoretical interpoint distance distribution (eq.(1)) and the empirical pair correlation function g can be intentionally shifted so as to agree with the *CSR* model by considering a reduced observation window. If we consider the R=423 μm device, effective radii of values R=400 μm and R=350 μm for the histogram (see Fig. 9.a) and for the pair correlation function (see Fig. 9.b), respectively, yield the expected results. The fact that these effective radii do not coincide indicates that the estimators for the non-homogeneous Poisson process we are dealing with cannot be simultaneously modified to yield the same *CSR* process. This difference is understandable, since the distance histogram is an overall measure of the point locations whereas the pair correlation function focuses mainly on the short length scale.

To conclude, it is worth mentioning that even though the ultimate reason for the non-uniform spot distribution has not been elucidated yet (it is still under investigation), additional experiments performed on rectangular area devices showed similar results (see Fig. 10). The spots are concentrated in the central region of the device area with the consequent lower density of filamentary paths in its periphery. This indicates that this not a shape-related device problem.

IV. CONCLUSION

In this work, the spatial distribution of filamentary current paths in circular area $Pt/HfO_2/Pt$ capacitors caused by the application of electrical stress was investigated. The study involved a number of statistical tools such as intensity plots, empirical and theoretical distance histograms as well as a functional summary estimator. The obtained results indicate that the widely accepted hypothesis of complete spatial randomness for the occurrence of failure events in MIM devices (and perhaps in MIS devices) does not always hold and that it should be thoroughly tested before its application. It was also shown that by considering an effective reduced device area, the estimators can be made compatible with a *CSR* process. However, caution should be exercised with this procedure since the effective device area required to do so may depend on the statistical estimator under consideration.

ACKNOWLEDGMENTS

E.M. acknowledges the support of the Spanish Ministry of Science and Technology under contract number TEC2009-09350 (partially funded by the European Union FEDER program) and the Departament d'Universitats, Recerca i Societat de la Informació de la Generalitat de Catalunya under contract number 2009SGR783. P.K.H. acknowledges the SFI grant ("09/IN.1/I2633 INVENT"). J.S. also acknowledges the ICREA ACADEMIA award. The authors also acknowledge D. O'Connell from Tyndall National Institute for samples processing.

REFERENCES

[1] J. Illian, A. Penttinen, H. Soyan, D. Stoyan, in *Statistical analysis and modelling of spatial point patterns*, Wiley, 2008

[2] E. Wu, J. Stathis, L. Han, "Ultra-thin oxide reliability for ULSI applications", Semicond Sci Technol 15, 425 (2000)

[3] E. Miranda, J. Suñé, "Electron transport through broken down ultra-thin SiO2 layers in MOS devices", Mic Rel 44, 1 (2004)

[4] J. Suñé, G. Mura, E. Miranda, "Are soft breakdown and hard breakdown of ultrathin gate oxides actually different failure mechanisms?, IEEE Electron Dev Letters 21, 167 (2000)

[5] H. David, H. Nagaraja, in *Order Statistics*, Wiley, New Jersey, 2003

[6] J. Suñé, E. Wu, "Statistics of successive breakdown events in gate oxides", IEEE Electron Dev Lett 24, 272 (2003)

[7] F. Monsieur, E. Vincent, D. Roy, S. Bruyere, J. C. Vildeuil, G. Pananakakis, G. Ghibaudo, "A thorough investigation of progressive breakdown in ultra-thin oxides. Physical understanding and application for industrial reliability assessment", IEEE International Reliability Physics Symposium 2002, pp. 45-54

[8] M. Alam, D. Varghese, B. Kaczer, "Theory of breakdown position determination by voltage- and current-ratio methods", IEEE Trans Elect Dev 55, 3150 (2008)

[9] A. Baddeley, R. Turner, "Spatstat: An R Package for Analyzing Spatial Point Patterns", J Stat Software 12, 1 (2005)

[10] P. Diggle, in *Statistical analysis of spatial point patterns*, Arnold, 2003

[11] H. Solomon, in *Geometric Probability*, Regional Conference Series in Applied Mathematics, Siam 28, 1978

[12] B. Eisenger, R. Sullivan, “Crofton’s differential equation”, The American Mathematical Monthly 107, 129 (2000)

FIGURE CAPTIONS

Fig. 1 – Experimental current-voltage characteristic showing the effects of the generation of multiple filamentary conduction paths. The marks on the top electrode of the capacitor shows the breakdown spot pattern.

Fig. 2 – Fresh and stressed devices with different areas. The spots were generated by the application of a voltage ramp as that shown in Fig. 1. R is the radius of the capacitor metal plate.

Fig. 3 – Empirical histograms and theoretical probability distributions (eq.(1)) for the interpoint distances in devices with different areas. The four smallest device areas are illustrated in Fig. 3.a, while Fig. 3.b shows the two largest device areas. Notice in this latest case the departure of the *CSR* model (solid lines) from the experimental data.

Fig. 4 – Empirical histograms and theoretical probability distributions (eq.(2)) for the nearest neighbor interpoint distances in devices with different areas. The four smallest device areas are illustrated in Fig. 4.a, while Fig. 4.b shows the two largest device areas. The departure of the *CSR* model (solid lines) from the experimental data is clearly visible in Fig. 4.b.

Fig. 5 – Experimental median interpoint distance as a function of the device radius (symbols). The solid line corresponds to the *CSR* model $M=0.905R$ [12]. N is the number of detected breakdown spots.

Fig. 6 – Local intensity plots for the same device (R=423 μm) calculated using different bandwidths (BW) for the Gaussian kernel. Notice the low density of spots close to the periphery of the device.

Fig. 7 – Radial distribution of spots as a function of the radius r (distance from the center of the disc). The solid line corresponds to the *CSR* model and is calculated using eq.(3). *a)* and *b)* corresponds to different stages of degradation of the same device (R=423 μm). The intensity plots show the spatial distribution of spots in either case.

Fig. 8 – Pair correlation function versus the interpoint distance for different device areas. The reference line (g=1) corresponds to the *CSR* model.

Fig. 9 – a) Interpoint distance histogram (R=423 μm) and theoretical probability distributions for R=423 μm and R=400 μm calculated using eq.(1). b) Pair correlation function as a function of the interpoint distance calculated using R=423 μm and R=350 μm.

Fig. 10 – Distribution of spots in a rectangular area device (2000 μm x 500 μm). Notice the accumulation of breakdown spots in the center of the device.

FIGURES

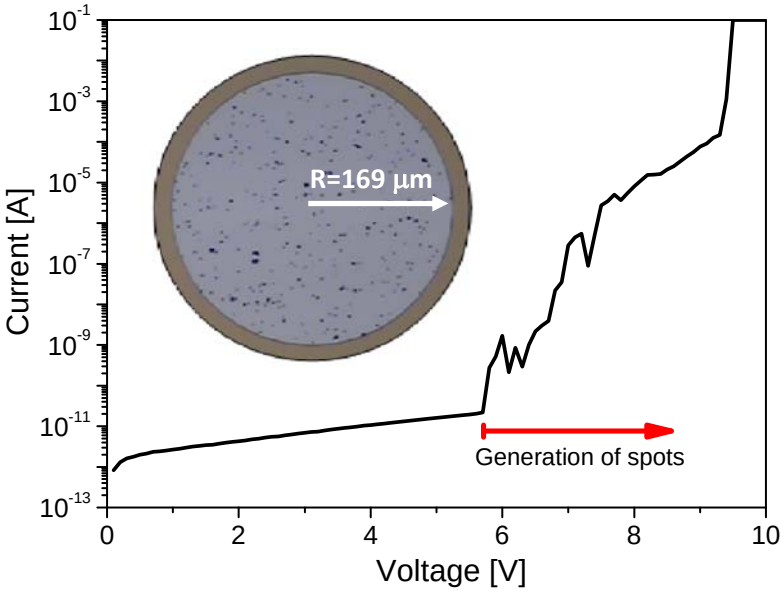

FIGURE 1

R	FRESH DEVICE	STRESSED DEVICE
113 µm	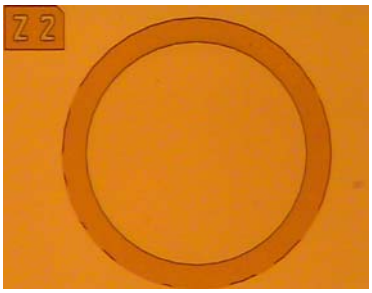	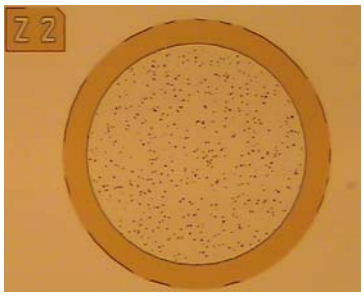
225 µm		
282 µm	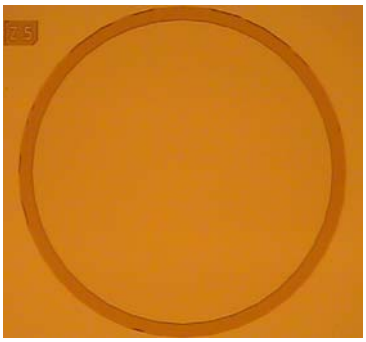	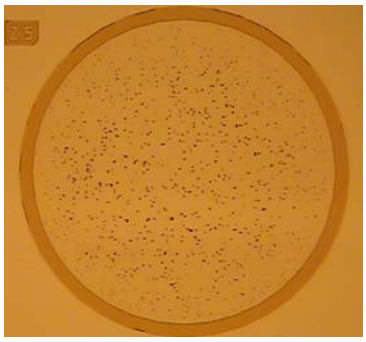
423 µm	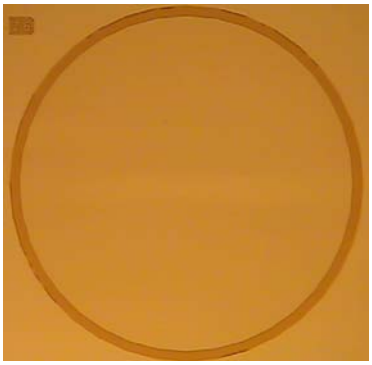	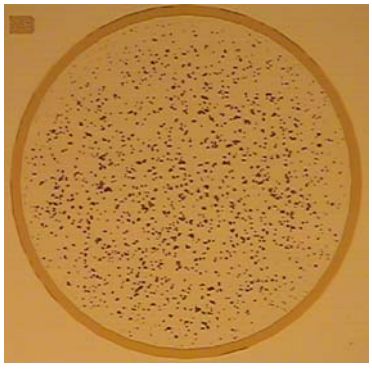

FIGURE 2

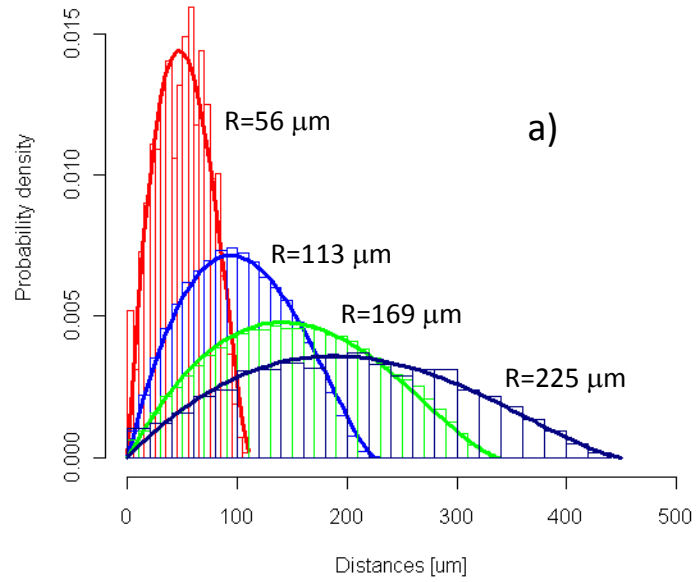
Probability density
0.000
0.005
0.010
0.015
R=56 µm
a)
R=113 µm
R=169 µm
R=225 µm
0
100
200
300
400
500
Distances [um]

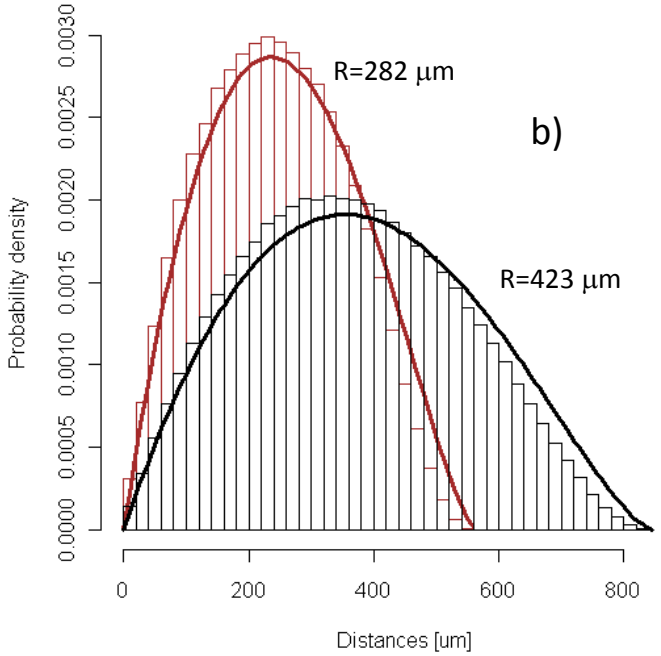
Probability density
0.0000
0.0005
0.0010
0.0015
0.0020
0.0025
0.0030
R=282 µm
b)
R=423 µm
0
200
400
600
800
Distances [um]

FIGURE 3

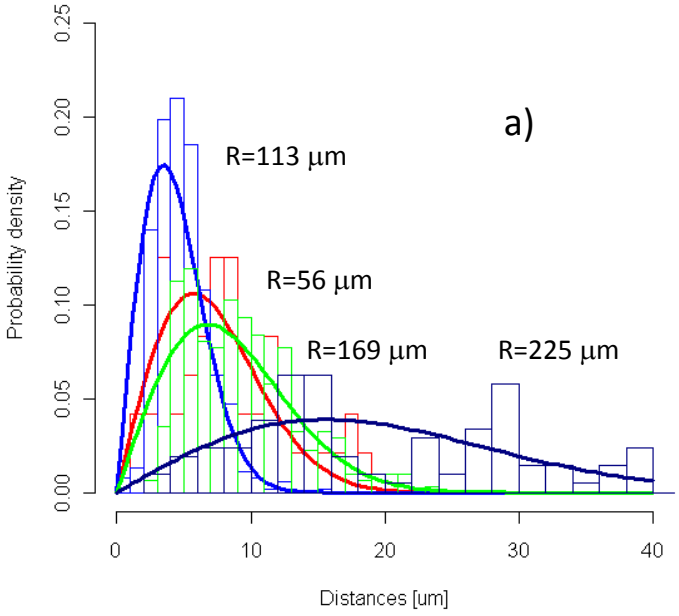
a)
R=113 µm
R=56 µm
R=169 µm
R=225 µm
Probability density
0.00
0.05
0.10
0.15
0.20
0.25
0
10
20
30
40
Distances [um]

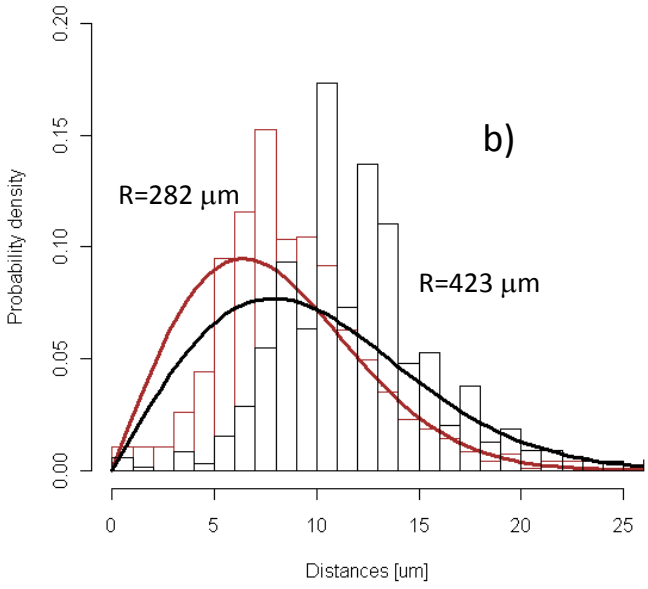
b)
R=282 µm
R=423 µm
Probability density
0.00
0.05
0.10
0.15
0.20
0
5
10
15
20
25
Distances [um]

FIGURE 4

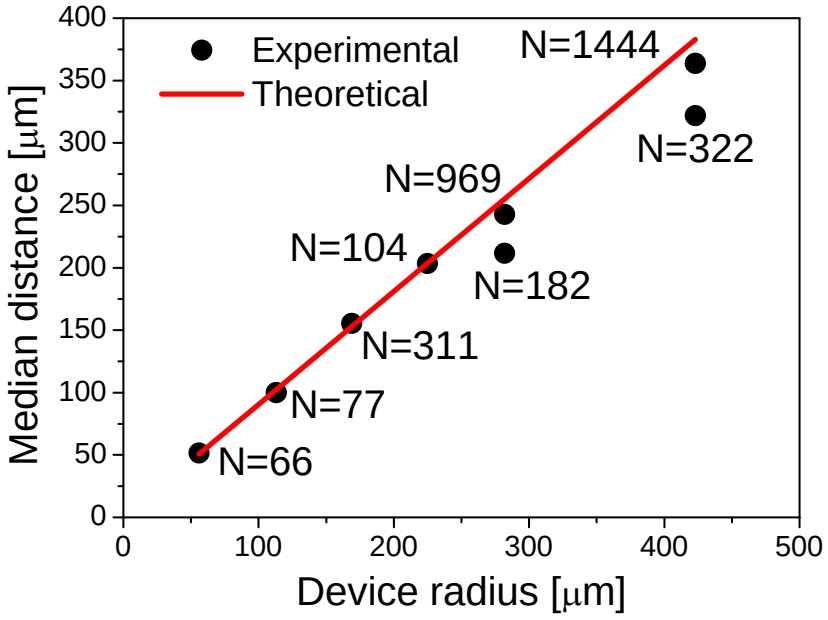
Experimental
Theoretical
N=1444
N=322
N=969
N=104
N=182
N=311
N=77
N=66
Median distance [μm]
Device radius [μm]
0
50
100
150
200
250
300
350
400
0
100
200
300
400
500

FIGURE 5

BW	Intensity Plot (R=423 μm)
10 μm	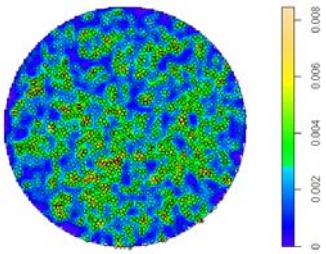
20 μm	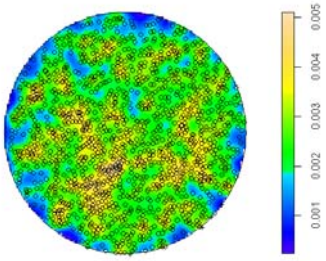
50 μm	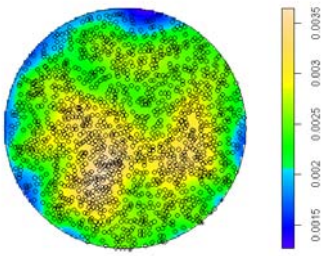
100 μm	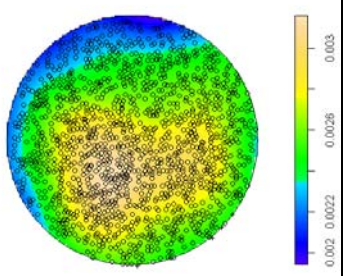

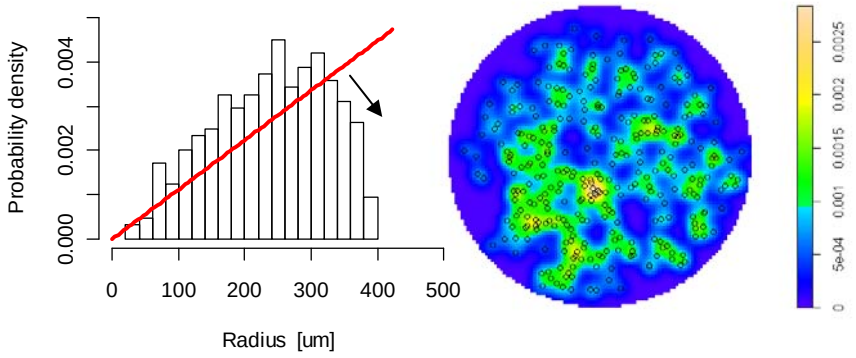
Probability density
0.000
0.002
0.004
0
100
200
300
400
500
Radius [um]
0
5e-04
0.001
0.0015
0.002
0.0025

a)

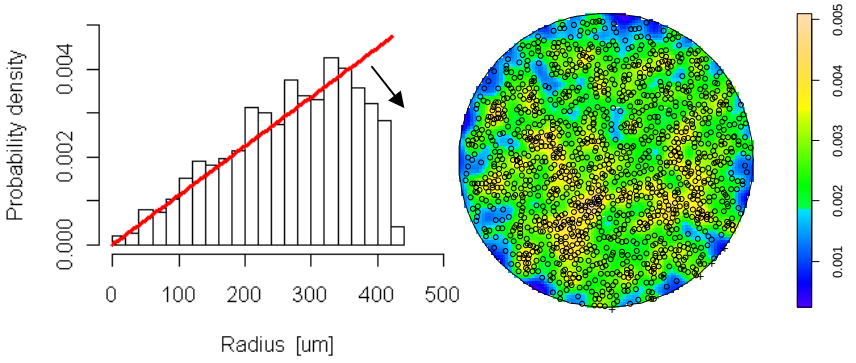
Probability density
0.000
0.002
0.004
0
100
200
300
400
500
Radius [um]
0.001
0.002
0.003
0.004
0.005

b)

FIGURE 7

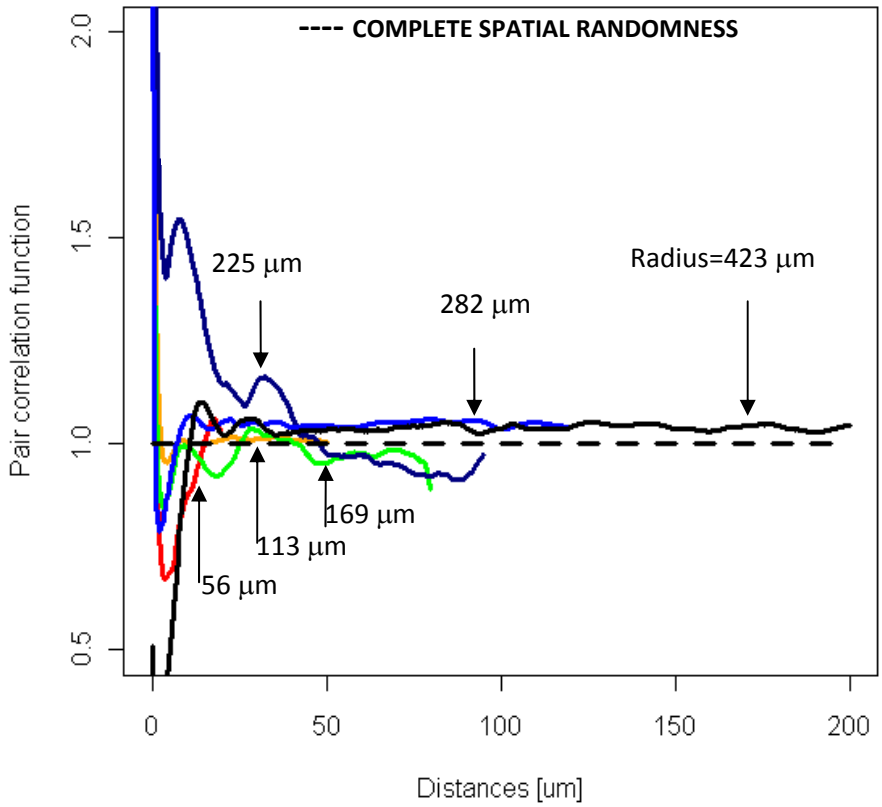
---- COMPLETE SPATIAL RANDOMNESS
225 µm
282 µm
Radius=423 µm
169 µm
113 µm
56 µm
Pair correlation function
0.5
1.0
1.5
2.0
0
50
100
150
200
Distances [um]

FIGURE 8

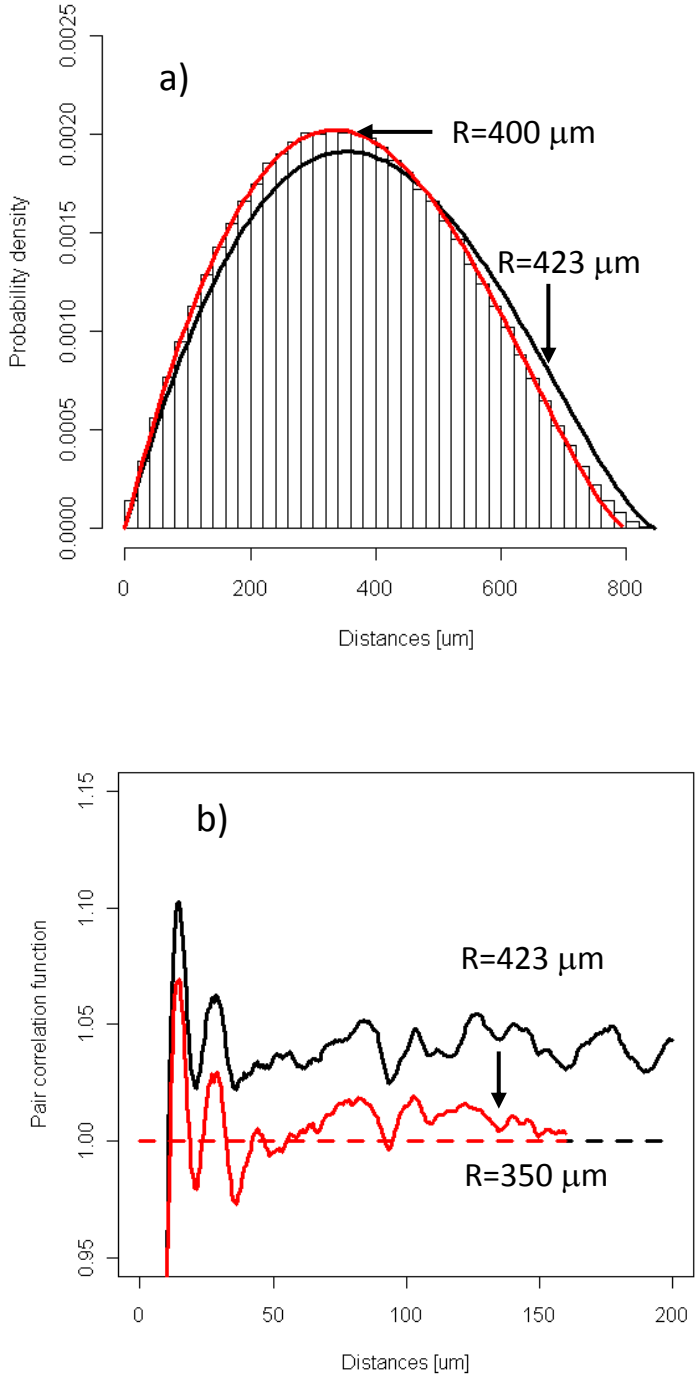
a)
R=400 µm
R=423 µm
Probability density
0.0000
0.0005
0.0010
0.0015
0.0020
0.0025
0
200
400
600
800
Distances [um]
b)
R=423 µm
R=350 µm
Pair correlation function
0.95
1.00
1.05
1.10
1.15
0
50
100
150
200
Distances [um]

FIGURE 9

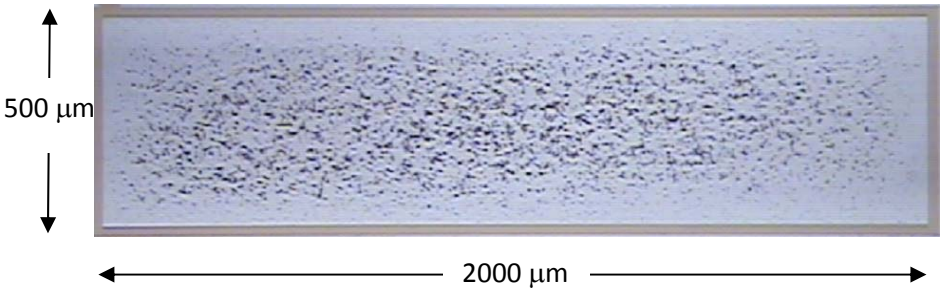

FIGURE 10